Journal of Energy Storage 106 (2025) 114758

Contents lists available at ScienceDirect

Journal of Energy Storage

journal homepage: www.elsevier.com/locate/est

Research papers

Heteroelectrocatalyst for optimizing polysulfides in high-efficiency Li—S batteries

Yuhang Lei [a], Lin Wu [a], Yafeng Li [a], Meijia Liu [a], Shuai Chen [a], Lin Tao [a,*], Lixiang Li [a], Chengguo Sun [a,b], Han Zhang [a,*], Baigang An [a,*]

[a] *Key Laboratory of Energy Materials and Electrochemistry Research Liaoning Province, School of Chemical Engineering, University of Science and Technology Liaoning, Anshan 114051, China*

[b] *School of Chemical Engineering, Nanjing University of Science and Technology, Nanjing 210094, China*

ARTICLE INFO

Keywords:
Li—S batteries
Polysulfides
MXene
Heteroelectrocatalyst
3D aerogel

ABSTRACT

Lithium-sulfur (Li—S) batteries are viewed as leading contender for future energy storage technologies, thanks to impressive energy density, extremely high theoretical capacity, abundant sulfur availability, and the inherently low reduction potential of lithium metal. These attributes make Li—S batteries highly appealing for advanced energy storage applications. Nonetheless, despite their promising potential, the real-world application of Li—S batteries is confronted with substantial obstacles. Foremost among these are the persistent shuttle effect of lithium polysulfides (LiPSs) at the sulfur cathode and the slow kinetics of sulfur reduction reactions, which together lead to poor rate performance and limited cycling stability. These issues significantly hinder their overall performance and commercial feasibility. Herein, a three-dimensional (3D) titanium-based heterostructure aerogel (MX-TiO_2) was prepared using a low-temperature hydrothermal method to serve as a sulfur host. Combining the adsorptive properties of TiO_2 with the catalytic capabilities of MXene, the MX-TiO_2 heteroelectrocatalyst facilitates seamless adsorption, diffusion, and conversion of polysulfides. When the heteroelectrocatalyst is used in the cathode, the corresponding Li—S cell maintains a discharge capacity retention of approximately 63 % over 150 cycles at 0.5C. Notably, MX-TiO_2 as the cathode material with an augmented sulfur loading of 5.42 mg cm^{-2}, the S/MX-TiO_2 cathode exhibits a notable initial capacity of 6.23 mAh cm^{-2} at 0.2C. This work presents a method for designing high-performance 3D heteroelectrocatalyst that simultaneously boost the catalytic conversion of polysulfides while mitigating the shuttle effect, approaching as a promising strategy for working out the fundamental challenges regarding lithium-sulfur batteries.

1. Introduction

The growing demand for electric vehicles, electronic devices, and grid energy storage solutions highlights the urgent need for advancement of next-generation, high-energy storage solutions [1–4]. Among secondary batteries, owing to their multiphase sulfur conversion mechanisms, lithium-sulfur (Li—S) batteries have garnered considerable interest as a viable contender for future energy storage systems. These batteries offer a notable energy density of 2600 Wh kg^{-1} along with an exceptional theoretical specific capacity reaching 1675 mAh g^{-1}, far surpassing traditional lithium-ion batteries in terms of performance potential [5–7]. Additionally, economic benefits and environmental benignity are attracting increasing attention [8]. Unfortunately, the real-world deployment of Li—S batteries faces ongoing challenges due to the shuttle effect of lithium polysulfides (LiPSs), causing inefficiencies in sulfur utilization. Furthermore, significant volume fluctuations during charge and discharge cycles, combined with sluggish sulfur redox kinetics, result in poor cycle life, limiting the widespread adoption of Li—S technology. These issues result in severe polarization, low Coulombic efficiency, poor utilization of active materials, and inferior cycling performance [9–12]. Consequently, the primary strategies to overcome these challenges focus on enhancing the catalytic conversion efficiency of sulfur species and suppressing shuttle effect.

In order to address aforementioned existing issues, various advanced sulfur host materials have been constructed, through physical and chemical confinement, to alleviate the shuttle effect of lithium polysulfides [13,14]. Among these materials, carbon-based structures are extensively employed as sulfur hosts, owing to their meticulously

---

* Corresponding authors.
E-mail addresses: taolin@ustl.edu.cn (L. Tao), hzhang0807@163.com (H. Zhang), bgan@ustl.edu.cn (B. An).

https://doi.org/10.1016/j.est.2024.114758
Received 19 September 2024; Received in revised form 29 October 2024; Accepted 20 November 2024

engineered porous architectures and excellent conductivity [15]. However, the lithium polysulfides' dissolution into the electrolyte is poorly regulated attributable to weak van der Waals interactions between polysulfides and carbon hosts, making these interactions insufficient for effective adsorption. Moreover, the high solubility of lithium polysulfides in certain ether-based solvents exacerbates the shuttle effect [16]. In contrast, metal compounds with strong polarity demonstrate a high adsorption capacity for polar lithium polysulfides due to their chemical bonding interactions [17]. Metal oxides, sulfides, phosphides, and nitrides demonstrate superior adsorption capacities for lithium polysulfides compared to conventional carbon materials [18,19]. Metal oxides, in particular, possess hydrophilic properties due to the presence of polar metal-oxygen bonds. For example, polar metal oxides such as TiO_2, MoO_2, CeO_2, V_2O_5, Fe_2O_3, and MnO_2 can form strong chemical bonds with lithium polysulfides [20–24].

In recent years, MXenes have gained widespread use in designing high-performance sulfur cathode materials because of their exceptional metallic conductivity, two-dimensional (2D) structure, abundant active edge sites, and tunable macroscopic structures [25–27]. MXenes, belonging to a class of two-dimensional layered materials composed of transition metal carbides or nitrides, are deemed as highly suitable conductive matrix materials. Their excellent electronic conductivity renders them ideal aimed at boosting the performance of Li—S batteries [28–30]. These materials provide an efficient solution to the intrinsic conductivity limitations of sulfur and its discharge products. Additionally, they help lower the reaction energy barriers encountered during the final solid-phase discharge processes, thereby improving the overall utilization efficiency of the active materials [31]. However, when MXenes are directly used as host materials, they cannot fully exploit their advantages. The tendency of stacking of two-dimensional nanosheets impedes the diffusion of Li^+ ions, as well as the decrease in specific surface area due to restacking obscures many surface active sites, resulting in the underutilization of active sites on MXene nanosheets [32]. It is challenging for a single catalyst host to simultaneously impart the advantages of adsorption of lithium polysulfides and their subsequent catalytic conversion in Li—S batteries [33]. Therefore, heteroelectrocatalyst are considered promising sulfur host materials [34,35]. Heteroelectrocatalyst leverages the synergistic effects of its constituent components, leading to significant enhancements in electron transfer, redox kinetics, and the adsorption of LiPSs in Li—S batteries [36].

In this investigation, a three-dimensional MX-TiO_2 aerogel was prepared via a low-temperature hydrothermal method to function as a sulfur hosting matrix in Li—S batteries. The 3D aerogel provides a scaffold for loading TiO_2 and MXene, inhibiting the stacking of MXene and preventing the masking of active sites. MXene enhance the efficient catalytic transformation of polysulfides while improving electrical conductivity of sulfur cathode, while, TiO_2 suppresses shuttle effect by increasing adsorption capacity of polysulfides. This synergistic heteroelectrocatalyst effectively mitigates the shuttle effect, accelerates internal redox reactions, and improves performance of Li—S batteries. The results indicate that the S/MX–TiO_2 cathode, with a high sulfur loading of 5.42 mg cm^{-2}, achieved a discharge capacity of 6.23 mAh cm^{-2} at 0.2C. This heteroelectrocatalyst presents new opportunities for electrochemical energy storage and catalysis, maintaining stable performance over 500 cycles.

2. Experimental section

2.1. Materials and characterization instrument

All chemicals were utilized as received, with no additional purification steps. Ti_3C_2 dispersions (5 mg mL^{-1}, Jilin 11 Technology Co., Ltd), Titanium dioxide powder (TiO_2, Aladdin), Graphene suspension (10 mg mL^{-1}, Suzhou Tanfeng Graphene Co.), Li—S electrolyte (LS-009, Suzhou Duoduo Chemical Technology Co.), Ethylenediamine (EDA, AR, 98 %, Shanghai Macklin Biochemical Technology Co., Ltd), Sulfur (S_8, Aladdin), and Super P conductive carbon black (Kejing Zhida Technology Co.).

The structural and morphological attributes of the samples were meticulously analyzed employing scanning electron microscopy (SEM) with the advanced Thermo Fisher Scientific Apreos system, and transmission electron microscopy (TEM) using the high-resolution Tecnai G2 F30 S-TWIN. For compositional and structural analysis, X-ray photoelectron spectroscopy (XPS) was executed with the KRATOS AXIS-SUPRA, while X-ray diffraction (XRD) assessments were conducted using the D8 ADVANCE instrument.

2.2. Synthesis of MX-TiO_2 aerogel

A 3 mL aliquot of Ti_3C_2 solution and 5 mg of TiO_2 powder were combined with 3 mL of graphene suspension and stirred extensively for 12 h. Subsequently, to achieve a total volume of 10 mL, 26.7 μL of ethylenediamine crosslinking agent and 4 mL of deionized water were added. The mixture was sonicated for 20 min, then heated in an oven at 95 °C for 6 h. Subsequently, it was transferred to a freeze dryer for 48 h for drying. Finally, the MX-TiO_2 aerogel was obtained. For comparison, pure MX aerogel and TiO_2 aerogel loaded on graphene were also prepared using a similar method.

2.3. Synthesis of MX-TiO_2 composites sulfur

The MX-TiO_2 powder was uniformly combined with elemental sulfur in a 1:2 ratio. Afterward, the mixture underwent thermal treatment at 155 °C for 12 h within an argon environment. Similarly, S/MX and S/TiO_2 composite materials were synthesized using the same method. The S/MX-TiO_2 electrode demonstrated superior wettability with the electrolyte, achieving a contact angle of around 7.9°. In contrast, the S/MX and S/TiO_2 electrodes exhibited slightly lower wettability, with contact angles measured at 9.8° and 13.1°, respectively (**Fig. S1**).

2.4. Electrochemical measurements and characterization

The electrochemical performance of the MX-TiO_2 composite, along with the pristine MX and TiO_2 materials as cathodes in lithium-sulfur cells, was assessed using the galvanostatic charge/discharge method. The electrodes for testing were fabricated by blending 70 wt% active materials with 20 wt% carbon black and 10 wt% polyvinylidene fluoride (PVDF) in *N*-methyl-2-pyrrolidone (NMP) to create a slurry. This slurry was then coated onto aluminum foil and subjected to a vacuum drying process at 60 °C for 12 h. The composite samples were meticulously fabricated into 2025 coin-type cells, with the assembly process conducted in a glove box under an argon atmosphere, where stringent control was exercised to keep water and oxygen concentrations below 0.1 ppm. The electrolyte composed of 1.0 M LiTFSI dissolved in a DOL and DME solvent mixture at a 1:1 volume ratio, with an added 1.0 wt% $LiNO_3$. Li—S batteries were carefully assembled using the prepared electrodes, a polypropylene separator, and lithium foil as the counter electrode. To evaluate electrochemical performance, galvanostatic charge/discharge tests were conducted with a Land CT2001A battery testing system, operating over a voltage range of 1.7 to 2.8 V. The sulfur loading was maintained within approximately 1.0–1.2 mg cm^{-2}, using 30 μL of electrolyte.

2.5. Li_2S_6 symmetric cell measurements

A slurry was prepared by thoroughly blending the catalyst material, carbon black, and PVDF in a precise weight ratio of 7:2:1. This mixture was evenly applied onto aluminum foil and subsequently dried under controlled conditions at 60 °C for a duration of 12 h to ensure complete solvent evaporation and proper adherence to the substrate. The material is punched into 12 mm diameter discs, achieving an areal mass loading of approximately 0.5 mg cm^{-2} for the catalyst. CR2025 symmetric cells were carefully assembled in a glovebox, where an argon atmosphere was maintained to strictly control moisture and oxygen levels, ensuring the integrity of the assembly process. The MX-TiO_2, MX and TiO_2 electrodes were used as both the cathode and the anode of a symmetrical cell. The electrolyte was prepared by dissolving 0.2 M Li_2S_6 and 1 M LiTFSI in a solvent blend of DME and DOL at a 1:1 volume ratio, with an additional 1 wt% $LiNO_3$ for enhancement. Symmetric cells were analyzed using cyclic voltammetry within a voltage window of −1.5 to 1.5 V, at a scan rate of 10 mV s^{-1}.

2.6. Measurement of the Li_2S nucleation

The cells were constructed using MX-TiO_2, MX, and TiO_2 as cathodes, with lithium foil serving as the anode. Each cell was provided with 15 μL of Li_2S_8 for the cathode compartment and an equal volume of 15 μL of LiTFSI electrolyte for the anode compartment. For the Li_2S precipitation evaluation, the cells underwent an initial galvanostatic discharge at a current density of 0.1 mA until the voltage declined to 2.06 V. Subsequently, they were subjected to potentiostatic discharge at a fixed potential of 2.05 V.

2.7. DFT calculation

All density functional theory (DFT) computations were conducted utilizing the Vienna Ab-initio Simulation Package (VASP), specifically version 5.4.4 [37]. The exchange-correlation interactions were described using the Perdew-Burke-Ernzerhof (PBE) functional, with ion-electron interactions managed through the Projector Augmented Wave (PAW) method [38,39] and a plane wave energy cutoff of 450 eV was employed, while van der Waals interactions were incorporated through the empirical DFT-D3 correction method [40]. The k-point meshes for the Brillouin zone were configured using the Monkhorst-Pack grid: 3 × 3 × 1 for the $Ti_2C_3O_2$ model, 2 × 2 × 1 for the $Ti_2C_3O_2$-TiO_2 models and 2 × 2 × 1 for the TiO_2 models. The convergence criteria were established at 0.01 eV $Å^{-1}$ for forces and 10^{-5} eV for energy. To avoid interlayer interactions, a vacuum spacing of 20 Å was introduced along the z-direction.

The free energy calculation of species adsorption (ΔG) is based on following equation.

$$\Delta G = \Delta E + \Delta E_{ZPE} - T\Delta S \quad (1)$$

Here, ΔE, ΔE_{ZPE}, and ΔS refer to the alterations in electronic energy, zero-point energy, and entropy, respectively, resulting from the adsorption of intermediates.

3. Result and discussion

Fig. 1a displays the microstructure diagram of the heterostructure MX-TiO_2. The heterostructure are uniformly supported on graphene oxide, facilitating rapid redox reactions of sulfur on the catalyst surface. As illustrated by digital photographs, the ultra-light porous aerogel, prepared via a low-temperature hydrothermal method, can easily stand on a dandelion, as shown in Fig. 1b. N_2 adsorption-desorption isotherms were utilized to examine the pore structure and surface area differences

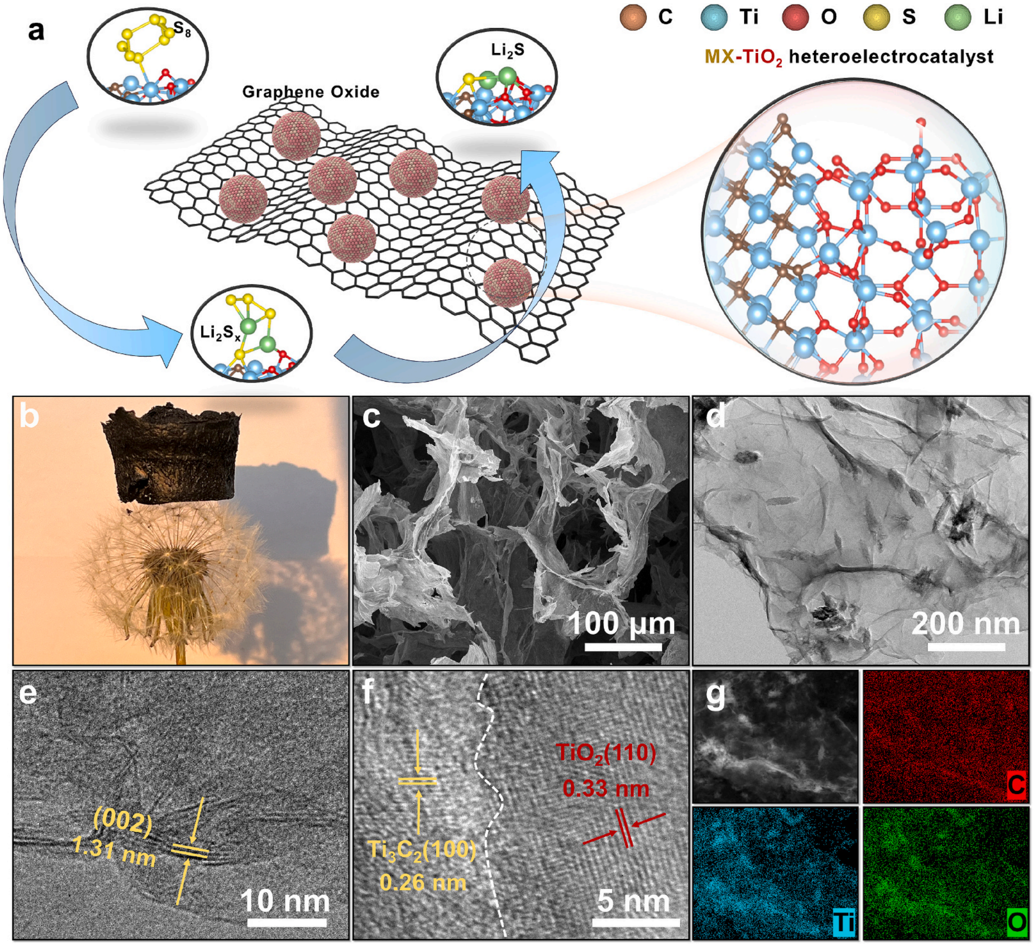

Fig. 1. a) Structure diagram of MX-TiO_2. b) Photograph showing the ultralight MX-TiO_2 aerogels positioned on a dandelion. SEM images of c) MX-TiO_2. TEM images of d-f) MX-TiO_2. g) High-angle annular dark field scanning transmission electron microscopy (HAADF-STEM) imaging, coupled with energy-dispersive X-ray spectroscopy (EDS) elemental mapping, was employed to characterize the MX-TiO_2 composite.

among MX-TiO_2, MX and TiO_2. The results indicated that the Brunauer-Emmett-Teller (BET) surface area of MX-TiO_2 is 44.5 $m^2\ g^{-1}$, exceeding that of MX (22.3 $m^2\ g^{-1}$) and TiO_2 (10.6 $m^2\ g^{-1}$). As shown in **Fig. S2**, the isotherms correspond to the IUPAC classification for type IV, featuring H4 hysteresis loops, which confirm the presence of mesopores in the MX-TiO_2. The morphological characteristics of the products were investigated using both scanning electron microscopy (SEM) and transmission electron microscopy (TEM). **Fig. S4** provides a detailed depiction of the pure graphene oxide aerogel, highlighting its intricate three-dimensional network architecture and structural features. After loading MX-TiO_2, the overall morphology retained this three-dimensional structure (Fig. 1c). **Fig. S5 and S6** showcase the SEM images and corresponding elemental mapping of MXene and TiO_2, respectively, offering insights into their morphological and compositional characteristics. Fig. 1d displays TEM images confirming the uniform dispersion of MX-TiO_2 heterostructure on high surface 3D aerogel. A high-resolution transmission electron microscopy (HR-TEM) visualization unveils a highly ordered crystalline arrangement with only four layers and an interlayer spacing of 1.31 nm (Fig. 1e). Furthermore, HR-TEM images reveal a tight interface between the (110) plane of TiO_2 and the (100) plane of MXene, with interplanar spacings within the crystal lattice of 0.33 nm and 0.26 nm, respectively (Fig. 1f) [41,42]. This indicates the successful preparation of the heterostructure aerogel. Corresponding elemental mapping illustrates the well-distributed C, Ti, and O on the GO substrate (Fig. 1g **and S3**). **Table S1** presents the elemental composition ratios of the three materials.

Structural transformations, elemental compositions, and valence states of the prepared samples were thoroughly examined through X-ray diffraction (XRD) and X-ray photoelectron spectroscopy (XPS) analyses. Fig. 2a illustrates that the XRD pattern validates the successful synthesis of the MX-TiO_2 phase, which aligns with the pure MX phase and the reference spectrum (JCPDS 21–1276) [43]. The MX-TiO_2 heterostructure exhibits characteristic diffraction peaks of pure MX at the (002) and (110) peak at a 2θ angle of 6.35° and 61.33°. Simultaneously, it matches perfectly with the standard spectrum of titanium dioxide. XPS analysis was utilized to comprehensively investigate alterations in the chemical bonding states and elemental compositions of MX-TiO_2, MX, and TiO_2, providing insights into the structural and compositional changes of these materials. The Ti 2p XPS spectra of MX, shown in **Fig. S7a**, reveal the Ti—C, Ti^{2+}, and Ti^{3+} peaks, consistent with previous findings [44]. The C 1 s spectrum (Fig. 2b) of the MX-TiO_2 aerogel displays four peaks: C—Ti at 282.8 eV, C—C at 284.6 eV, C—O at 285.6 eV, and C=O at 287.1 eV [45]. The C 1 s spectrum of MX reveals three distinct peaks at 284.8, 286.6, and 288.1 eV, which are attributed to C—C, C—O, and O-C=O bonds, respectively, reflecting the diverse carbon bonding environments present in the material (Fig. 2c) [46]. The Ti 2p XPS spectra of MX-TiO_2 display binding energy peaks at 455.6 eV and 458.5 eV, corresponding to Ti—C and Ti—O interactions, respectively (Fig. 2d), indicating the structural integrity of MX nanosheets in the MX-TiO_2 hybrid [44]. The peaks attributed to Ti—C, Ti^{2+}, and Ti^{3+} were detected, showing a resemblance to those found in MX. Additionally, two more peaks corresponding to Ti—O (459.0 eV, 464.7 eV), originate from TiO_2 (**Fig. S7b**) [47]. These findings validate the successful fabrication of the MX-TiO_2 heterostructure.

To shed light on the electrocatalytic behavior and bidirectional LiPSs conversion efficiency of MX-TiO_2, a comprehensive suite of electroanalytic measurements was conducted. To evaluate the enhanced redox kinetics of MX-TiO_2, cyclic voltammetry (CV) profiles of the sulfur cathodes were systematically acquired over a voltage range extending from 1.7 to 2.8 V, utilizing a scan rate of 0.1 mV s^{-1}. (**Fig. 3a**). The S/

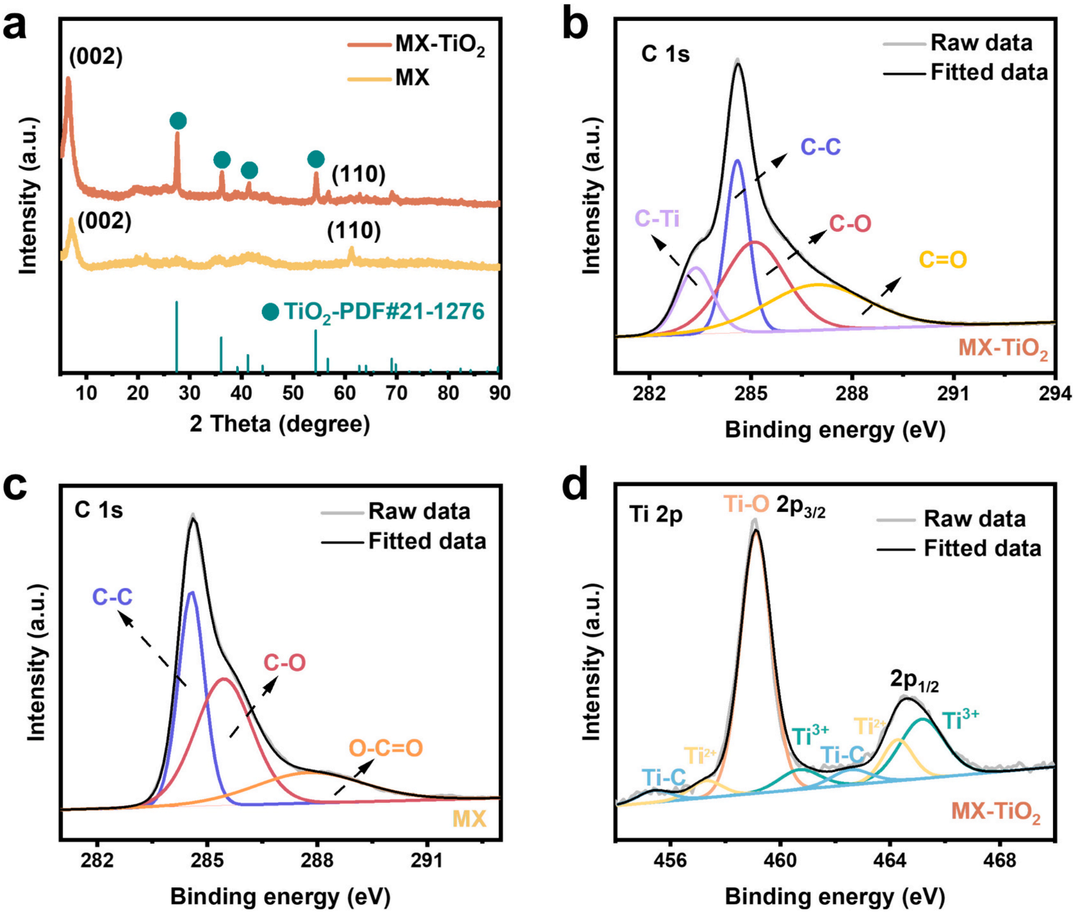

Fig. 2. a) XRD patterns for MX-TiO_2 and MX. b, c) Detailed C 1 s XPS spectra for MX-TiO_2 and MX. d) Precise Ti 2p XPS spectrum for MX-TiO_2.

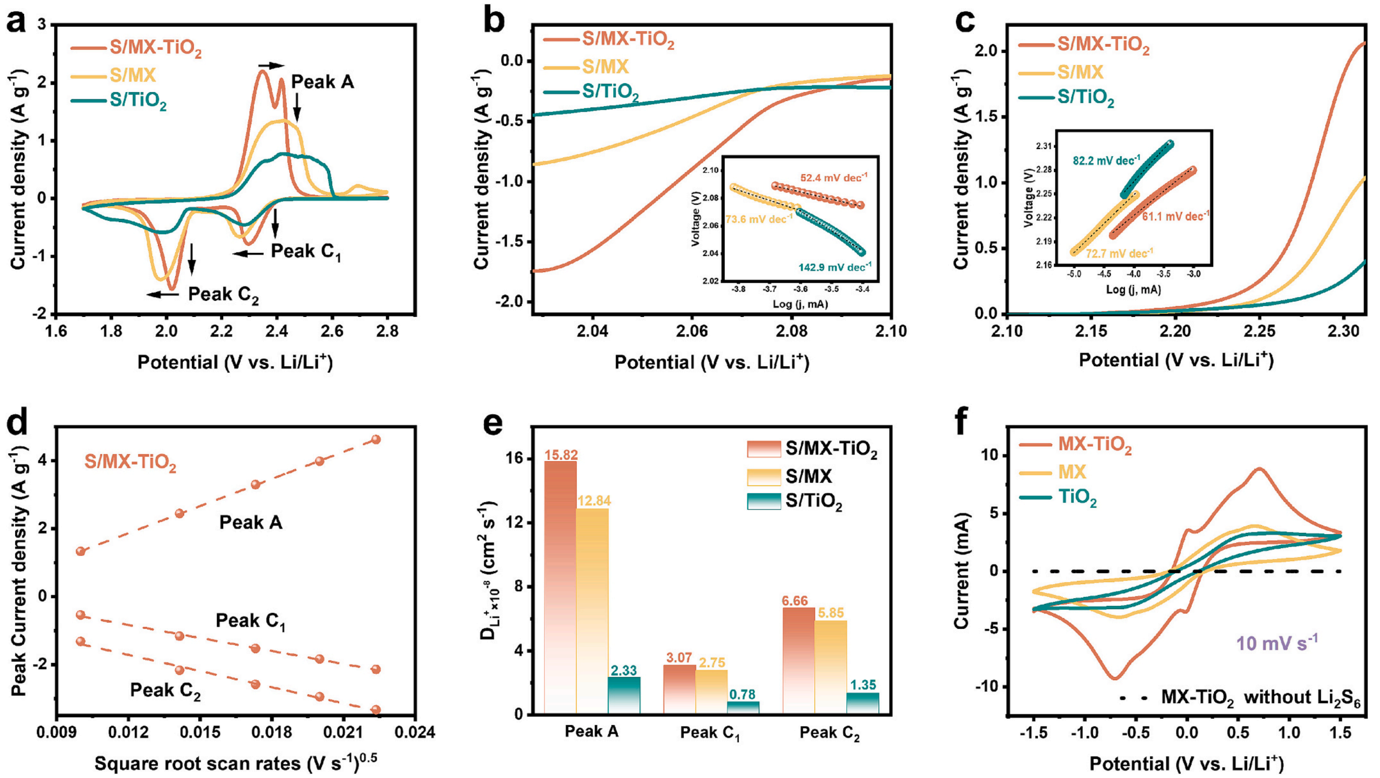

Fig. 3. a-c) Cycling voltammetry profiles for S/MX-TiO$_2$, S/MX and S/TiO$_2$ cathodes (inset: Tafel plots for corresponding oxidation and reduction reactions). d) Peak currents plotted against the square root of scan rates for S/MX-TiO$_2$. e) The Li$^+$ diffusion coefficients for the processes indicated by peaks A, C$_1$, and C$_2$ were determined for the S/MX-TiO$_2$, S/MX, and S/TiO$_2$ cathodes. f) Cyclic voltammograms of symmetric cells with MX-TiO$_2$, MX, and TiO$_2$ electrodes, measurements were conducted at a scan rate of 10 mV s^{-1} for both conditions, with and without the Li$_2$S$_6$ solution.

MX-TiO$_2$ electrode displays higher reaction potential and peak current during the cathodic sweeps (Peaks C$_1$ and C$_2$) and exhibits markedly narrower and more pronounced profiles in the anodic sweep (Peak A) compared to the S/MX and S/TiO$_2$, suggesting substantially enhanced reactions at these potentials. Additionally, the Tafel slopes of both reduction (from Li$_2$S$_4$ to Li$_2$S) and oxidation (from Li$_2$S to Li$_2$S$_8$) peaks were derived to quantify the catalytic activities [48]. As depicted in Fig. 3**b and** 3**c**, the Tafel slopes for MX-TiO$_2$ are 52.4 and 61.1 mV dec^{-1}, significantly lower than those for MX (73.6 and 72.7 mV dec^{-1}) and TiO$_2$ (142.9 and 82.2 mV dec^{-1}), indicating notable bidirectional electrocatalytic activity.

The Li-ion transfer kinetics were assessed to examine the electrocatalytic impact on polysulfide redox kinetics. As illustrated in **Fig. S8**, the Li-ion diffusion coefficient was determined through a series of continuous CV measurements performed across scanning speeds from 0.1 to 0.5 mV s^{-1} [49]. The CV curve of MX-TiO$_2$ exhibited sharper peaks and smaller peak shifts compared to MX and TiO$_2$, indicating a faster transition between sulfur and polysulfides [50,51]. The dynamics of lithium-ion diffusion were elucidated through the application of the Randles-Sevcik equation, which facilitated a detailed analysis of the electrochemical behavior:

$$I_{peak} = \left(2.69 \times 10^{5}\right) n^{1.5} A D_{Li^{+}}^{0.5} \upsilon^{0.5} C_{Li} \tag{2}$$

the relationship between the curve and the parameters in the equation reveals a direct correlation with the rate of lithium-ion diffusion [52]. The Fig. 3**d and S8** depict the correlation between the square root of the scan rate ($\upsilon^{0.5}$) and peak current (I_{peak}), demonstrating a linear relationship. The linear fitting of the data reveals that the S/MX-TiO$_2$ cathode exhibits significantly steeper slopes, reflecting the highest Li$^+$ diffusion rates across all peaks. This result provides additional evidence that the MX-TiO$_2$ heteroelectrocatalyst sites significantly enhance the kinetics of LiPSs conversion. As shown in Fig. 3**e**, for the S/MX-TiO$_2$ cathode, the diffusion coefficients of lithium ions (D_{Li}^{+}) are calculated as 3.07×10^{-8} cm^2 s^{-1} at peak C$_1$, 6.66×10^{-8} cm^2 s^{-1} at peak C$_2$, and 15.82×10^{-8} cm^2 s^{-1} at peak A. These values are notably higher compared to those recorded for the S/MX cathode (2.75×10^{-8} to 12.84×10^{-8} cm^2 s^{-1}) and the S/TiO$_2$ cathode (0.78×10^{-8} to 2.33×10^{-8} cm^2 s^{-1}), which indicates significantly faster diffusion and reaction kinetics on the MX-TiO$_2$ surface. It further confirms the superior electrocatalytic performance of the robust MX-TiO$_2$ heteroelectrocatalyst in promoting sulfur redox reactions.

To evaluate the electrocatalytic properties of MX-TiO$_2$, a symmetric cell was assembled using identical electrode materials for both the anode and cathode (Fig. 3**f**). The cyclic voltammetry profiles for the Li$_2$S$_6$-symmetric cells revealed distinctive redox behavior: MX-TiO$_2$ exhibited two separate sets of redox peaks, while MX and TiO$_2$ showed only a single pair of reversible peaks. These experiments were performed over a voltage interval extending from −1.5 to 1.5 V, employing a scan rate of 10 mV s^{-1}. Specifically, the anodic peaks observed signify the transition from Li$_2$S$_2$/Li$_2$S to long-chain Li$_2$S$_6$, followed by the oxidation of Li$_2$S$_6$ to elemental sulfur. Conversely, the cathodic peaks represent the reduction of S$_8$ to Li$_2$S$_6$ and the subsequent transformation to Li$_2$S. Compared to the MX and TiO$_2$ electrodes, the MX-TiO$_2$ electrode displays progressively narrower redox peaks and reduced peak separations, which underscores its superior sulfur electrocatalytic performance. Remarkably, the MX-TiO$_2$ heteroelectrocatalyst cell achieves both the highest current and the most distinct redox peaks, reflecting optimal sulfur utilization and efficient conversion. This improvement is ascribed to the refined electronic configuration of the active sites, which is enhanced by the heterostructure [53].

Generally, nucleation and growth of Li$_2$S are influenced by the reactive interfaces of the host materials [54]. To validate the synergistic effect of the MX-TiO$_2$ heteroelectrocatalyst, Li$_2$S deposition experiments were conducted on various surfaces. As shown in Fig. 4**a-c**, the Li$_2$S

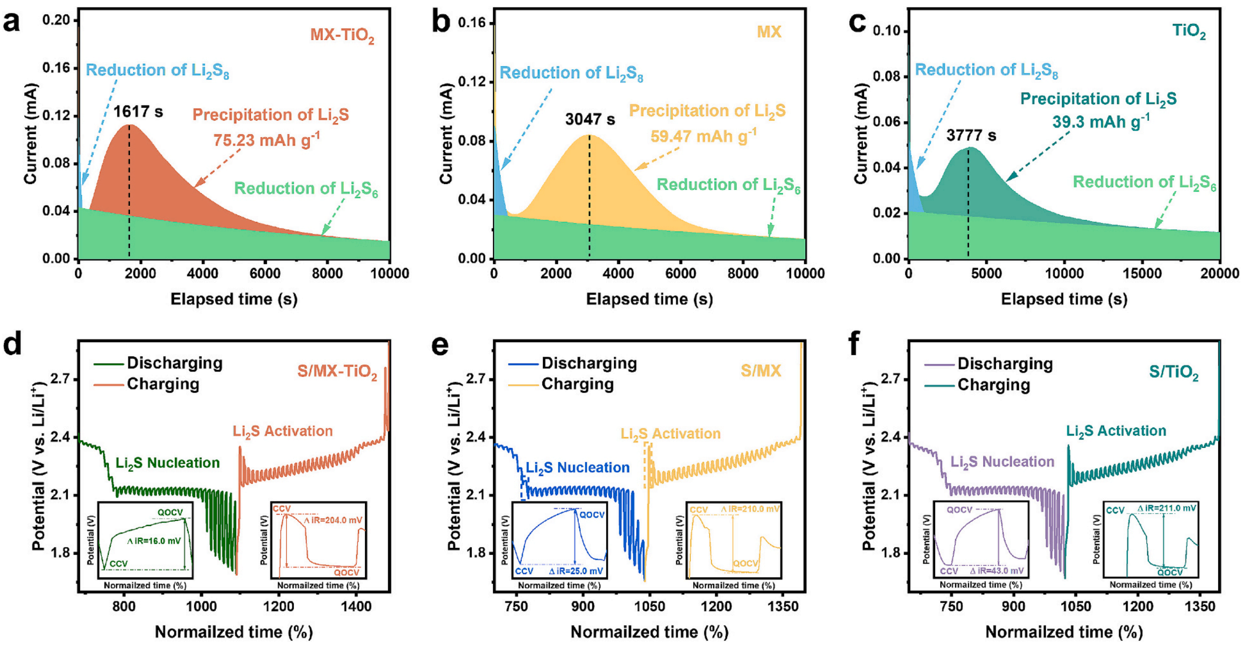

Fig. 4. a-c) Nucleation tests of Li_2S using different electrodes to assess nucleation kinetics. d-f) The galvanostatic intermittent titration technique (GITT) was employed to generate profiles for Li—S batteries equipped with MX-TiO_2, MX, and TiO_2 cathodes, all evaluated under a current density of 0.1C.

precipitation capacity on MX-TiO_2 (75.2 mAh g^{-1}) significantly surpasses that of MX (59.5 mAh g^{-1}) and TiO_2 (39.3 mAh g^{-1}). Additionally, Li_2S nucleation occurs earlier on MX-TiO_2 than on the MX and TiO_2 surfaces, indicating its superior catalytic effect on the LiPS transformation process. These results demonstrate that the MX-TiO_2 heterostructure significantly reduces the overpotential required for Li_2S nucleation and enhances interfacial electron transfer kinetics during Li_2S precipitation [55,56].

Fig. 4**d-f** present the voltage profiles obtained from galvanostatic intermittent titration technique (GITT) analysis for S/MX-TiO_2, S/MX, and S/TiO_2. The profiles clearly exhibit two distinct discharge plateaus and a single charging plateau. The upper discharge plateau corresponds to the transformation of insulating sulfur into long-chain lithium polysulfides (Li_2S_n, $4 \leq n \leq 8$). In contrast, the lower discharge plateau is associated with the reduction of these long-chain polysulfides to insoluble Li_2S_2 and Li_2S. The charging plateau reflects the reoxidation process, during which insoluble Li_2S_2/Li_2S is converted back to elemental sulfur. The potential measured after rest is referred to as the quasi open-circuit voltage (QOCV), while the potential during current application is known as the closed-circuit voltage (CCV). Internal resistances were calculated using the following formula:

$$\Delta iR_{internal} = \frac{|\Delta V_{QOCV-CCV}|}{I_{applied}} \tag{3}$$

As illustrated in Fig. 4**d-f**, S/MX-TiO_2 displayed an obvious lower internal resistance at the Li_2S nucleation and Li_2S activation point (ΔiR = 16.0 mV) and charge (ΔiR = 204.0 mV) compared to the S/MX cathode (discharge: 25.0 mV, charge: 210.0 mV) and the S/TiO_2 cathode (discharge: 43.0 mV, charge: 211.0 mV), highlighting the high electric conductivity and enhanced Li_2S nucleation kinetics on heteroelectrocatalyst [57–59].

The pronounced shuttle effect leads to substantial capacity decay in Li—S batteries, with surface adsorption playing a crucial role in facilitating electrocatalytic conversion reactions. In particular, the adsorption capacity of the host material stands as a key performance indicator for lithium-sulfur batteries. To assess this, a static adsorption test was conducted, comparing the adsorption capacities of MX-TiO_2, MX, and TiO_2 in Li_2S_6 solutions under consistent mass conditions. As shown in Fig. 5a, MX-TiO_2 causes the solution to transition from a dark yellow to almost colorless, whereas MX only reduces the color intensity to yellow and the solution in the TiO_2 sample changed from deep yellow to absolutely colorless. Comparative analysis confirms that the addition of TiO_2 provides significant advantages for MX-TiO_2 in terms of chemical adsorption and anchoring ability to LiPSs, thereby inhibiting the dissolution and diffusion of LiPSs.

Moreover, XPS analysis was utilized to explore the interactions between MX-TiO_2 and lithium polysulfides. As depicted in Fig. 5b, the Ti $2p_{2/3}$ peaks of MX-TiO_2 shift towards lower binding energies after interaction with Li_2S_6 solution, indicating polysulfides electron migration to Ti in MX-TiO_2 [60]. The observation of Ti—S bond formation at 456.6 eV suggests strong chemical interactions between MX-TiO_2 heteroelectrocatalyst and LiPSs [61]. This is due to the robust Lewis acid-base interaction between the vacant orbitals of the surface Ti atoms and the electronegative polysulfide ions [62]. Furthermore, the S 2p spectrum displays distinct peaks corresponding to thiosulfate and polythionate at around 168.8 and 170.0 eV, respectively (Fig. 5c), indicating that MX-TiO_2 can oxidize soluble LiPSs to insoluble thiosulfate and polythionate, facilitating immobilization and subsequent conversion of polysulfides [63].

Density functional theory (DFT) simulations were conducted to better elucidate how the combined components of MX-TiO_2 work together to improve battery performance. Changes in typical charge densities were examined to illustrate how S_8 interacts with MXene or the heterostructure, as shown in Fig. 5d-e. The charge density accumulation around S_8 and the corresponding charge depletion at the heterostructure enhance the interaction between sulfur and titanium atoms, making these interactions more pronounced compared to those with MXene alone [64,65]. Additionally, the investigation into how the combined components affect battery performance included an analysis of the variations in Gibbs free energy (ΔG) during the sulfur reduction process on TiO_2, MXene and MX-TiO_2 heterostructure surfaces were calculated (Fig. 5f). Molecular structure diagrams of different sulfur species on the MX-TiO_2 heterostructure, MX and TiO_2 are shown in **Fig. S9, Fig. S10 and Fig. S11**, respectively. The reaction converting S_8 to Li_2S_8 was observed to be spontaneously exothermic. The free energy transition from Li_2S_2 to Li_2S represents the most considerable non-spontaneous reaction, identifying this step as a rate-determining factor in the discharge process [66,67]. The free energy associated with the rate-

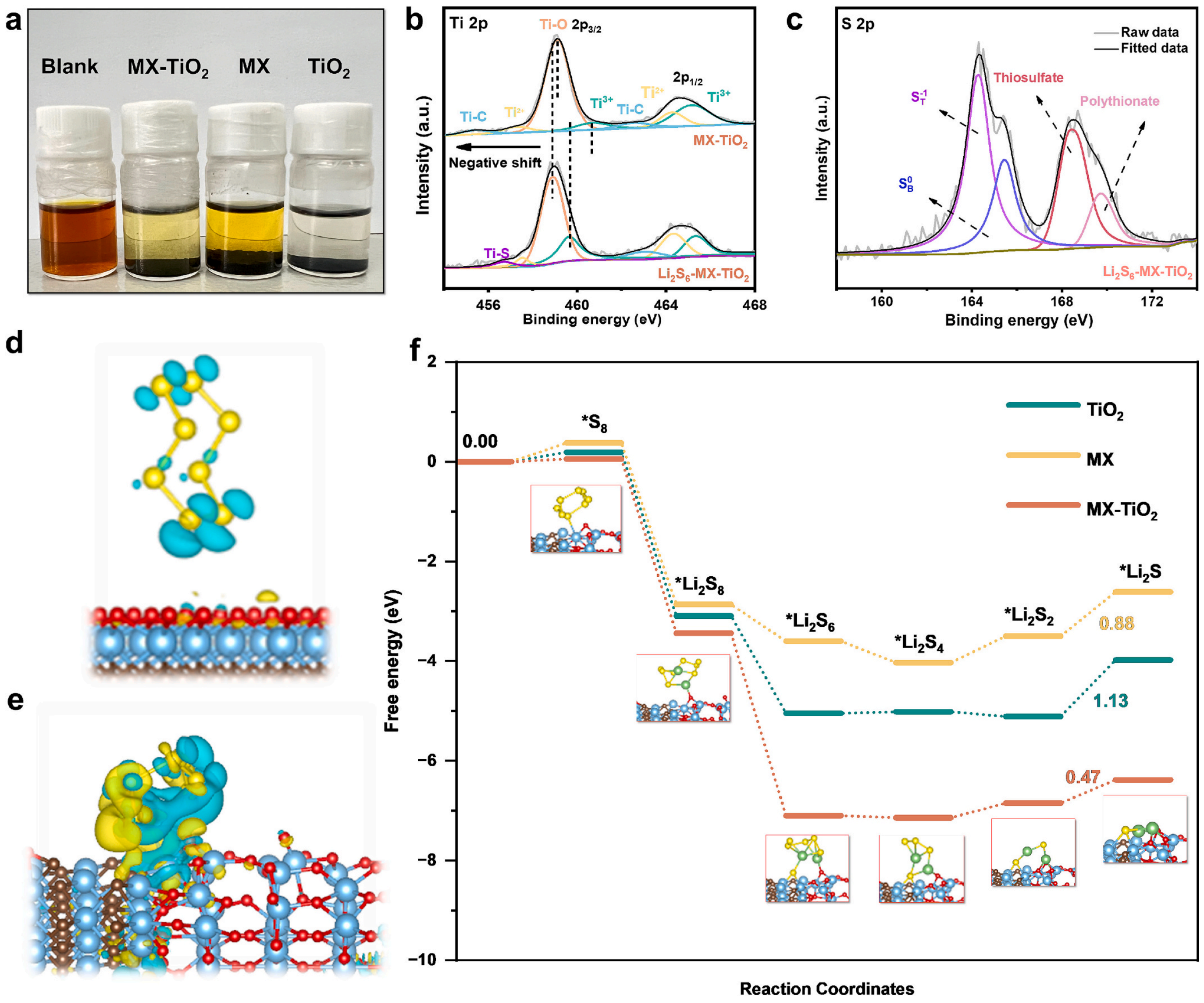

Fig. 5. a) Digital images of MX-TiO$_2$, MX and TiO$_2$ samples immersed in Li$_2$S$_6$ solution. b) XPS profiles of Ti 2p and c) S 2p for MX-TiO$_2$ after interaction with Li$_2$S$_6$ solution. d) Differential charge density diagrams for MX and e) MX-TiO$_2$. f) Gibbs free energy diagrams illustrating the multiphase sulfur conversion mechanisms on MX-TiO$_2$, MX and TiO$_2$ surfaces.

limiting reduction step was 0.47 eV for MX-TiO$_2$, which is notably lower than the 1.13 eV observed for TiO$_2$ and the 0.88 eV for MX. This suggests that the MX-TiO$_2$ heterostructure facilitates a more thermodynamically favorable sulfur reduction process compared to TiO$_2$ and MX.

As demonstrated in Fig. 6a, the initial assessment of the S/MX-TiO$_2$ electrode's electrochemical characteristics revealed a remarkable capacity of 1584.7 mAh g^{-1} at 0.1C rate. This performance notably surpasses that of the S/MX and S/TiO$_2$ electrodes, which exhibited capacities of 1078 mAh g^{-1} and 1063.3 mAh g^{-1}, respectively. Beginning with the second cycle, the S/MX-TiO$_2$ electrode exhibited a gradual capacity decline from 1330.8 mAh g^{-1} to 654.6 mAh g^{-1} over the course of 150 cycles, maintaining an impressive capacity retention of 63 %. In contrast, the discharge capacities of S/MX and S/TiO$_2$ decreased to 551.7 mAh g^{-1} and 388.9 mAh g^{-1}, respectively, after the same number of cycles. Furthermore, the initial Coulombic efficiency of the S/MX-TiO$_2$ electrode was markedly superior at 92.40 % compared to 86.59 % for the S/TiO$_2$ material. These findings suggest that the heteroelectrocatalyst effectively mitigates the polysulfide shuttle effect, confining the active species within the cathode region and thereby enhancing cycling stability. Meanwhile, **Fig. S12** presents the typical galvanostatic charge-discharge curves for S/MX-TiO$_2$, S/MX, and S/TiO$_2$ at a rate of 0.5C. Notably, the voltage profiles show minimal variation after 150 cycles, underscoring the superior structural stability of the S/MX-TiO$_2$ electrode during cycling. At the end of the battery discharge process, despite the reduction of long-chain LiPSs into shorter chains, the electrolytes in both the S/TiO$_2$ and S/MX systems retain a yellow color, indicating significant amounts of dissolved polysulfides. In contrast, the electrolyte in the S/MX-TiO$_2$ system remains nearly colorless throughout discharge (**Fig. S13a**), underscoring the S/MX-TiO$_2$ catalyst's exceptional efficiency in confining LiPSs within the cathode region during both charge and discharge. The minimal presence of dissolved polysulfides on the separator further visually confirms the heteroelectrocatalyst's superior ability to reduce polysulfide shuttling. To verify the structural stability of the heteroelectrocatalyst after cycling, SEM imaging and EDS elemental mapping were conducted on the S/MX-TiO$_2$ cathode after 150 cycles. As shown in **Fig. S13b-c**, sulfur exhibits a uniform dendritic deposition on the cathode surface, with elemental mapping revealing an even distribution of sulfur across the catalyst, highlighting the remarkable stability of the heteroelectrocatalyst material during cycling. The galvanostatic charge/

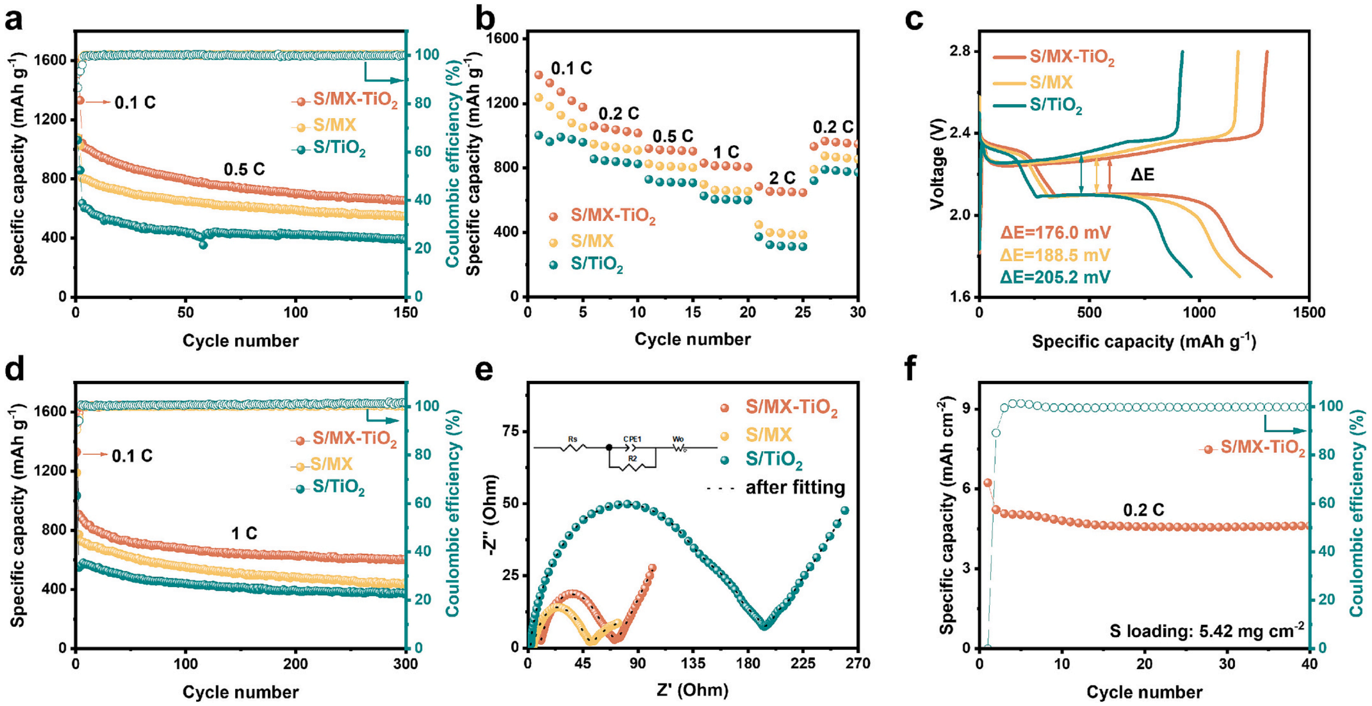

Fig. 6. Assessment of Li—S battery performance across various cathode materials: a) Cycle stability at 0.5C, b) rate performance, c) discharge and charge curves at 0.1C, d) prolonged cycling capability at a 1C rate, e) Nyquist plots, and f) performance of the S/MX-TiO$_2$ cathode at a rate of 0.2C with a high sulfur loading of 5.42 mg cm^{-2}.

discharge (GCD) profiles reveal that the discharge plateau around 2.0 V is indicative of the reduction process where soluble long-chain Li_2S_n ($4 \leq n \leq 8$) are transformed into less soluble species such as Li_2S_2 and Li_2S. In contrast, the overlapping charge plateaus observed between 2.2 and 2.4 V correspond to the oxidation of Li_2S_2 and Li_2S back into higher polysulfides like Li_2S_8 or elemental sulfur (S8), highlighting the reverse redox transformation [68,69]. The S/MX-TiO$_2$ electrode exhibited impressive discharge capacities across a wide array of current densities, extending from 0.1C to 2C and rapidly returned to 0.2C (Fig. 6b). At various current densities, including 0.1C, 0.2C, 0.5C, 1C, and 2C, the recorded discharge capacities were 1377.2, 1060.4, 920.4, 830.5, and 685.5 mAh g^{-1}, respectively. Following a reversion to 0.2C, the cell achieved a stable discharge capacity of 933.7 mAh g^{-1}. This performance was compared with data from the literature, as illustrated in **Fig. S14**. The S/MX-TiO$_2$ electrode demonstrates the lowest polarization potential of 176.0 mV among the three electrodes, in contrast to S/MX (188.5 mV) and S/TiO$_2$ (205.2 mV) at 0.1C (Fig. 6c), demonstrating that MX-TiO$_2$ can not only improve sulfur utilization but also reduce the polarization potential of the electrode. Additionally, the overall charge-discharge profile of S/MX-TiO$_2$ demonstrates exceptional stability, showing no significant change in voltage polarization (**Fig. S15**). Even at 2C, the two distinct discharge platforms remain visible, indicating that S/MX-TiO$_2$ not only surpasses S/MX and S/TiO$_2$ in catalytic efficiency and reaction kinetics but also exhibits superior catalytic stability. To assess their long-term cycling durability, the cells were subjected to a rigorous evaluation at a charge/discharge rate of 1C over extended periods, as shown in Fig. 6d. After 300 cycles, the S/MX-TiO$_2$ cell sustained a substantial rechargeable capacity of 607.4 mAh g^{-1}, demonstrating a capacity maintenance of 66.9 % and a decay rate of 0.11 %.

To examine the improvement in sulfur redox kinetics provided by S/MX-TiO$_2$, as shown in Fig. 6e, electrochemical impedance spectroscopy (EIS) was performed. The EIS results indicate that the S/MX-TiO$_2$ electrode exhibits the smallest charge-transfer resistance (R_{ct}) among all the samples evaluated. After forming a heterostructure with TiO$_2$, the resistance of the S/MX-TiO$_2$ electrode does not significantly increase and remains much lower than that of the S/TiO$_2$ electrode. This indicates that the MX-TiO$_2$ interface facilitates rapid charge transfer and efficient sulfur redox kinetics [70]. To further evaluate the catalytic activity of MX-TiO$_2$, we conducted post-cycling EIS measurements and compared them with pre-cycling EIS data. As shown in **Fig. S16**, the post-cycling S/MX-TiO$_2$ cathode displays the smallest semicircle in the high-frequency region, indicating that MX-TiO$_2$ provides abundant metallic active sites, accelerates the activation of both sulfur and lithium sulfide, and enhances the interfacial redox kinetics of polysulfides. Assessing the potential for practical use of Li—S batteries also hinges on their discharge performance under conditions of augmented sulfur layer density. In Fig. 6f, even with an augmented sulfur loading of 5.42 mg cm^{-2}, the S/MX-TiO$_2$ cathode exhibits a notable initial capacity of 6.23 mAh cm^{-2} at 0.2C. It maintains a capacity of 4.62 mAh cm^{-2} after 40 cycles, with a per-cycle capacity decay rate of only 0.64 %, demonstrating remarkable cycling stability throughout the testing period. This performance highlights the effectiveness of MX-TiO$_2$ as a cathode host, demonstrating its ability to substantially mitigate the shuttle effect and thereby elevate the overall operational efficiency of Li—S batteries [71]. The high-capacity retention and robust cycling stability under high sulfur loading conditions suggest that MX-TiO$_2$ could be a valuable material for advancing the real-world deployment of Li—S batteries within advanced energy storage frameworks.

Fig. 7 illustrates that while TiO$_2$ exhibits strong adsorption of LiPSs, its catalytic activity is limited, leading to suboptimal polysulfide conversion. This strong adsorption also impedes the transport dynamics of LiPSs and the permeation of Li$^+$ ions, thereby slowing down the redox kinetics. Conversely, MXene excels at accelerating the catalytic conversion of polysulfides but suffers from inadequate polysulfide adsorption, resulting in a significant shuttle effect. In contrast, the titanium-based heteroelectrocatalyst combines the advantages of both TiO$_2$ and MXene, facilitating rapid and efficient bidirectional sulfur redox reactions. This integrated approach not only ensures rapid conversion of LiPSs but also effectively mitigates the shuttle effect, maintaining its performance even with high sulfur loading.

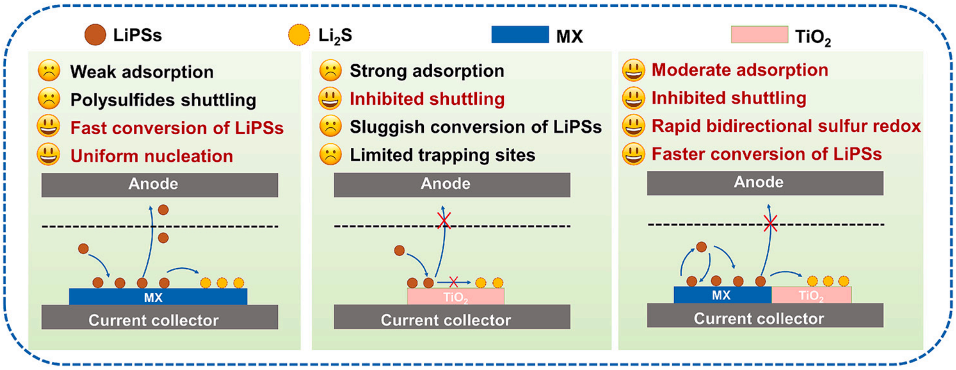

Fig. 7. Diagram illustrating the polysulfide adsorption and transformation mechanisms on MX, TiO_2, and MX-TiO_2.

4. Conclusion

In this study, we successfully synthesized Li—S battery cathode materials comprising titanium-based heteroelectrocatalyst using a low-temperature hydrothermal method. The synergistic catalysis exhibited excellent electrochemical performance. MXene demonstrated substantial catalytic prowess, significantly accelerating the redox reaction kinetics, while TiO_2 played a crucial role in the adsorption of lithium polysulfides. This dual-functional approach effectively mitigates the shuttle effect while concurrently bolstering the overall cycling stability of the system, contributing to a more robust and reliable performance. Insights from DFT calculations, corroborated by experimental data, demonstrate that the MX-TiO_2 heteroelectrocatalyst adeptly merges strong adsorption properties with exceptional catalytic performance. This combination facilitates an efficient, uninterrupted process for adsorption, diffusion, and transformation of polysulfides. Consequently, battery exhibits outstanding performance metrics, exhibiting a peak discharge capacity of 1584.7 mAh g^{-1} at a 0.5C rate, this configuration also demonstrates a noteworthy endurance, maintaining 66.9 % of its capacity over 300 cycles at 1C. This research introduces a streamlined methodology for fabricating superior efficiency Li—S batteries and offers valuable perspectives on advancing their commercial application.

CRediT authorship contribution statement

Yuhang Lei: Writing – review & editing, Writing – original draft, Methodology, Data curation. **Lin Wu:** Visualization, Investigation, Formal analysis. **Yafeng Li:** Data curation, Conceptualization. **Meijia Liu:** Visualization, Formal analysis. **Shuai Chen:** Visualization, Methodology. **Lin Tao:** Supervision, Software. **Lixiang Li:** Supervision, Project administration. **Chengguo Sun:** Supervision, Project administration. **Han Zhang:** Writing – review & editing, Supervision, Project administration, Funding acquisition. **Baigang An:** Resources, Funding acquisition.

Declaration of competing interest

The authors declare no competing financial interest.

Acknowledgements

The authors gratefully acknowledge financial supported by the National Natural Science Foundation of China (22109061, 11972178, 52304330 and 51972156), the Nature Science Foundation of Liaoning Province (2022-BS-283), and Technology Liaoning Project Grants (601010326). Key Project supported by the Research Foundation of Education Bureau of Liaoning Province (No. JYTZD2023093), Distinguished Professor Project of Education Department of Liaoning and the Open Project Found of Key Laboratory of Energy Materials and Electrochemistry Liaoning Province are acknowledged.

Appendix A. Supplementary data

Supplementary data to this article can be found online at https://doi.org/10.1016/j.est.2024.114758.

Data availability

Data will be made available on request.

References

[1] Y. Li, J. Zhang, Q. Chen, X. Xia, M. Chen, Emerging of heterostructure materials in energy storage: a review, Adv. Mater. 33 (2021) 2100855.
[2] D. Larcher, J.-M. Tarascon, Towards greener and more sustainable batteries for electrical energy storage, Nat. Chem. 7 (2015) 19–29.
[3] R. Fang, S. Zhao, Z. Sun, D.W. Wang, H.M. Cheng, F. Li, More reliable lithium-sulfur batteries: status, solutions and prospects, Adv. Mater. 29 (2017) 1606823.
[4] A. Manthiram, Y. Fu, S.-H. Chung, C. Zu, Y.-S. Su, Rechargeable lithium–sulfur batteries, Chem. Rev. 114 (2014) 11751–11787.
[5] P.G. Bruce, S.A. Freunberger, L.J. Hardwick, J.-M. Tarascon, Li–O_2 and Li–S batteries with high energy storage, Nat. Mater. 11 (2012) 19–29.
[6] J. Han, H. Li, D. Kong, C. Zhang, Y. Tao, H. Li, Q.-H. Yang, L. Chen, Realizing high volumetric lithium storage by compact and mechanically stable anode designs, ACS Energy Letters 5 (2020) 1986–1995.
[7] M. Zhao, Y.-Q. Peng, B.-Q. Li, X.-Q. Zhang, J.-Q. Huang, Regulation of carbon distribution to construct high-sulfur-content cathode in lithium–sulfur batteries, journal of energy, Chemistry 56 (2021) 203–208.
[8] D. Lu, X. Wang, Y. Hu, L. Yue, Z. Shao, W. Zhou, L. Chen, W. Wang, Y. Li, Expediting stepwise sulfur conversion via spontaneous built-in electric field and binary sulfiphilic effect of conductive NbB_2-MXene heterostructure in lithium–sulfur batteries, Adv. Funct. Mater. 33 (2023) 2212689.
[9] M. Wild, L. O'neill, T. Zhang, R. Purkayastha, G. Minton, M. Marinescu, G. Offer, Lithium sulfur batteries, a mechanistic review, Energy Environ. Sci. 8 (2015) 3477–3494.
[10] H.J. Peng, J.Q. Huang, X.B. Cheng, Q. Zhang, Review on high-loading and high-energy lithium–sulfur batteries, Adv. Energy Mater. 7 (2017) 1700260.
[11] L. Zhou, D.L. Danilov, F. Qiao, J. Wang, H. Li, R.A. Eichel, P.H. Notten, Sulfur reduction reaction in lithium–sulfur batteries: mechanisms, catalysts, and characterization, Adv. Energy Mater. 12 (2022) 2202094.
[12] Y. Guo, R. Khatoon, J. Lu, Q. He, X. Gao, X. Yang, X. Hu, Y. Wu, J. Lian, Z. Li, Regulating adsorption ability toward polysulfides in a porous carbon/Cu_3P hybrid for an ultrastable high-temperature lithium–sulfur battery, carbon, Energy 3 (2021) 841–855.
[13] D. Gueon, M.-Y. Ju, J.H. Moon, Complete encapsulation of sulfur through interfacial energy control of sulfur solutions for high-performance Li–S batteries, Proc. Natl. Acad. Sci. 117 (2020) 12686–12692.
[14] Y. Li, R. Yang, J. Xie, J. Li, H. Huang, X. Liang, D. Huang, Z. Lan, H. Liu, G. Li, S. Xu, J. Guo, W. Zhou, Potassium Ion–Assisted Self–Assembled MXene-K-CNT Composite as High–Quality Sulfur–Loaded Hosts for Lithium–Sulfur Batteries, ACS Appl. Mater. Interfaces 16 (2024) 39771–39783.
[15] J. Lee, J.H. Moon, Polyhedral TiO_2 particle-based cathode for Li-S batteries with high volumetric capacity and high performance in lean electrolyte, Chem. Eng. J. 399 (2020) 125670.
[16] H. Wang, T. Zhou, D. Li, H. Gao, G. Gao, A. Du, H. Liu, Z. Guo, Ultrathin Cobaltosic oxide Nanosheets as an effective sulfur encapsulation matrix with strong affinity toward Polysulfides, ACS Appl. Mater. Interfaces 9 (2016) 4320–4325.
[17] N. Wang, B. Chen, K. Qin, E. Liu, C. Shi, C. He, N. Zhao, Rational design of Co_9S_8/CoO heterostructures with well-defined interfaces for lithium sulfur batteries: a

study of synergistic adsorption-electrocatalysis function, Nano Energy 60 (2019) 332–339.

[18] J. He, Y. Chen, A. Manthiram, Vertical Co_9S_8 hollow nanowall arrays grown on a Celgard separator as a multifunctional polysulfide barrier for high-performance Li–S batteries, Energy Environ. Sci. 11 (2018) 2560–2568.

[19] S. Ghashghaie, S.H. Cheng, J. Fang, H. Shahzad, G. Muhyodin, H. Liu, C. Liu, R. L. Ma, C. Chung, Unique flake-shaped sulfur morphology favored by the binder-free electrophoretically deposited TiO_2 layer as a promising cathode structure for Li-S batteries, J. Alloys Compd. 176907 (2024).

[20] Y. Lu, T. Liu, Fe_2O_3 nano particles embedded Fe_2O_3/BP2000 composite for Li-S battery, J. Porous. Mater. (2024) 1–9.

[21] X. Sun, S. Gao, J. Wang, X. Qiu, Y. Ma, G. Xu, X. Song, TiO_2 modified Para-aramid nanofiber composite separator for thermal runaway prevention and shuttle effect mitigation of lithium-sulfur batteries, Microporous Mesoporous Mater. 366 (2024) 112983.

[22] Y.-S. Liu, X. Liu, S.-M. Xu, Y.-L. Bai, C. Ma, W.-L. Bai, X.-Y. Wu, X. Wei, K.-X. Wang, J.-S. Chen, 3D ordered macroporous MoO_2 attached on carbonized cloth for high performance free-standing binder-free lithium–sulfur electrodes, J. Mater. Chem. A 7 (2019) 24524–24531.

[23] X. Tao, Z. Yang, M. Cheng, R. Yan, F. Chen, S. Cao, S. Li, T. Ma, C. Cheng, W. Yang, Phosphorus modulated porous CeO_2 nanocrystallines for accelerated polysulfide catalysis in advanced Li-S batteries, J. Mater. Sci. Technol. 131 (2022) 212–220.

[24] Y.-T. Gao, X.-Y. Wang, D.-Q. Cai, S.-Y. Zhou, S.-X. Zhao, Enhanced Polysulfide Trapping and Conversion by Amorphous–Crystalline Heterostructured MnO_2 Interlayers for Li-S Batteries, ACS Appl. Mater. Interfaces, 15 (2023) 30152–30160.

[25] L. Cheng, R. Tian, Y. Zhao, Z. Wei, X. Pu, Y.-L. Zhu, D. Zhang, F. Du, Small things make a big difference: conductive cross-linking sodium alginate@MXene binder enables high-volumetric-capacity and high-mass-loading Li–S battery, Nano Lett. 23 (2023) 10538–10544.

[26] K. Yang, C. Li, H. Qi, Y. Dai, Y. Cui, Y. He, Developing a MXene quantum dot-based separator for Li–S batteries, J. Mater. Chem. A 11 (2023) 10425–10434.

[27] Q. Liang, S. Wang, X. Lu, X. Jia, J. Yang, F. Liang, Q. Xie, C. Yang, J. Qian, H. Song, R. Chen, High-entropy MXene as bifunctional mediator toward advanced Li–S full batteries, ACS Nano 18 (2024) 2395–2408.

[28] T. Li, Y. Liu, J. Wang, H. Hao, Z. Yu, H. Liu, Constructing metal telluride-grafted MXene as electron "donor–acceptor" heterostructure for accelerating redox kinetics of high-efficiency Li–S batteries, J. Mater. Chem. A 12 (2024) 12691–12701.

[29] W. Zhang, H. Pan, N. Han, S. Feng, X. Zhang, W. Guo, P. Tan, S. Xie, Z. Zhou, Q. Ma, Balancing adsorption, catalysis, and desorption in cathode catalyst for Li–S batteries, Adv. Energy Mater. 13 (2023) 2301551.

[30] S. Xu, Y. Zhang, Y. Shi, Q. Qian, C. Wang, J. Qiu, Enhancing the cycling stability of Li-S batteries with flexible freestanding sulfur cathodes through a spider-hunting strategy, Chem. Eng. J. 479 (2024) 147869.

[31] Y. Chen, Y. Liao, Y. Wu, L. Li, Z. Zhang, S. Luo, Y. Wu, Y. Qing, Configuring single-layer MXene nanosheet onto natural wood fiber via C–Ti–C covalent bonds for high-stability Li-S batteries, Journal of Energy Chemistry, 95 (2024) 701–711.

[32] J. Song, X. Guo, J. Zhang, Y. Chen, C. Zhang, L. Luo, F. Wang, G. Wang, Rational design of free-standing 3D porous MXene/rGO hybrid aerogels as polysulfide reservoirs for high-energy lithium–sulfur batteries, J. Mater. Chem. A 7 (2019) 6507–6513.

[33] Y. Li, Q. Zhang, S. Shen, S. Wang, L. Shi, D. Liu, Y. Fu, D. He, Multi-perspective synergistic construction of dual-functional heterostructures for high-temperature Li-S batteries, Chem. Eng. J. 468 (2023) 143562.

[34] Q. Liang, S. Wang, X. Jia, J. Yang, Y. Li, D. Shao, L. Feng, J. Liao, H. Song, MXene derivative Ta_4C_3-Ta_2O_5 heterostructure as bi-functional barrier for Li-S batteries, J. Mater. Sci. Technol. 151 (2023) 89–98.

[35] B. Yang, M. Xu, Y. Gao, Q. Zhu, B. Xu, Interfacial engineering and coupling of MXene/reduced graphene oxide/C_3N_4 aerogel with optimized d-band center as a free-standing sulfur carrier for high-performance Li-S batteries, Small Methods 8 (2024) 2301102.

[36] P. Cheng, L. Shi, W. Li, X. Fang, D. Cao, Y. Zhao, P. Cao, D. Liu, D. He, Efficient regulation of Polysulfides by MoS_2/MoO_3 Heterostructures for high-performance Li-S batteries, Small 19 (2023) 2206083.

[37] G. Kresse, J. Furthmüller, Efficient iterative schemes for ab initio total-energy calculations using a plane-wave basis set, Phys. Rev. B 54 (1996) 11169.

[38] J.P. Perdew, K. Burke, M. Ernzerhof, Generalized gradient approximation made simple, Phys. Rev. Lett. 77 (1996) 3865.

[39] B. Hammer, L.B. Hansen, J.K. Nørskov, Improved adsorption energetics within density-functional theory using revised Perdew-Burke-Ernzerhof functionals, Phys. Rev. B 59 (1999) 7413.

[40] S. Grimme, Semiempirical GGA-type density functional constructed with a long-range dispersion correction, J. Comput. Chem. 27 (2006) 1787–1799.

[41] K. Wei, J.-X. Yang, F.-Y. Bai, Y.-S. Shen, K. Liu, J. Liu, L.-H. Chen, Y. Li, B.-L. Su, In situ conversion of Ti_3C_2 MXene to Sandwich Ti_3C_2/R-TiO_2 for promoted photocatalytic hydrogen production, ACS Applied Energy Materials 6 (2023) 5456–5463.

[42] K. Zhao, J. Liu, X. Wang, Q. Che, B. Zhang, H. He, K. Wang, Y. Chen, 90% yield production of Spiropyran covalently grafted MXene-based RRAM devices for optoelectronic dual-response switching, Advanced Optical Materials 12 (2024) 2301761.

[43] C. Ma, M. Wei, $BiVO_4$-nanorod-decorated rutile/anatase TiO_2 nanofibers with enhanced photoelectrochemical performance, Mater. Lett. 259 (2020) 126849.

[44] H. Zhang, Y. Zhang, L. Li, H. Zhou, M. Wang, L. Li, X. Geng, B. An, C. Sun, A rational design of titanium-based heterostructures as electrocatalyst for boosted conversion kinetics of polysulfides in Li-S batteries, J. Colloid Interface Sci. 633 (2023) 432–440.

[45] S. Zhang, H. Liu, B. Cao, Q. Zhu, P. Zhang, X. Zhang, R. Chen, F. Wu, B. Xu, An MXene/ CNTs@P nanohybrid with stable Ti–O–P bonds for enhanced lithium ion storage, J. Mater. Chem. A 7 (2019) 21766–21773.

[46] J. Liu, W. Lu, X. Lu, L. Zhang, H. Dong, Y. Li, Versatile $Ti_3C_2T_x$ MXene for free-radical scavenging, Nano Res. 15 (2021) 2558–2566.

[47] L. Ma, Y. Zhang, S. Zhang, L. Wang, C. Zhang, Y. Chen, Q. Wu, L. Chen, L. Zhou, W. Wei, Integrating energy band alignment and oxygen vacancies engineering of TiO_2 Anatase/rutile Homojunction for kinetics-enhanced Li–S batteries, Adv. Funct. Mater. 33 (2023) 2305788.

[48] L. Jiao, C. Zhang, C. Geng, S. Wu, H. Li, W. Lv, Y. Tao, Z. Chen, G. Zhou, J. Li, Capture and catalytic conversion of polysulfides by in situ built TiO_2-MXene heterostructures for lithium–sulfur batteries, Adv. Energy Mater. 9 (2019) 1900219.

[49] R. Luo, Q. Yu, Y. Lu, M. Zhang, T. Peng, H. Yan, X. Liu, J.-K. Kim, Y. Luo, 3D pomegranate-like TiN@graphene composites with electrochemical reaction chambers as sulfur hosts for ultralong-life lithium–sulfur batteries, Nanoscale Horizons 4 (2019) 531–539.

[50] K. Zhang, Z. Zhao, X. Wang, Ni_2P/rGO as a highly efficient sulfur host toward enhancing the polysulfides redox for lithium-sulfur batteries, J. Alloys Compd. 906 (2022) 164376.

[51] X. Geng, C. Liu, C. Zhao, Z. Jiang, E.G. Lim, Y. Wang, I. Mitrovic, L. Yang, P. Song, Sulfydryl-modified MXene as a sulfur host for highly stable Li-S batteries, Electrochim. Acta 441 (2023) 141877.

[52] M. Zhao, Y. Lu, Y. Yang, M. Zhang, Z. Yue, N. Zhang, T. Peng, X. Liu, Y. Luo, A vanadium-based oxide-nitride heterostructure as a multifunctional sulfur host for advanced Li-S batteries, Nanoscale 13 (2021) 13085–13094.

[53] J. Cai, Z. Sun, W. Cai, N. Wei, Y. Fan, Z. Liu, Q. Zhang, J. Sun, A robust ternary heterostructured electrocatalyst with conformal graphene chainmail for expediting Bi-directional sulfur redox in Li–S batteries, Adv. Funct. Mater. 31 (2021) 2100586.

[54] S. Wu, W. Wang, J. Shan, X. Wang, D. Lu, J. Zhu, Z. Liu, L. Yue, Y. Li, Conductive 1T-VS_2-MXene heterostructured bidirectional electrocatalyst enabling compact Li-S batteries with high volumetric and areal capacity, Energy Storage Materials 49 (2022) 153–163.

[55] V.P. Nguyen, I.H. Kim, H.C. Shim, J.S. Park, J.M. Yuk, J.-H. Kim, D. Kim, S.-M. Lee, Porous carbon textile decorated with VC/V_2O_3-X hybrid nanoparticles: dual-functional host for flexible Li-S full batteries, Energy Storage Materials 46 (2022) 542–552.

[56] H. Li, R. Gao, B. Chen, C. Zhou, F. Shao, H. Wei, Z. Han, N. Hu, G. Zhou, Vacancy-rich MoSSe with sulfiphilicity–lithiophilicity dual function for kinetics-enhanced and dendrite-free Li-S batteries, Nano Lett. 22 (2022) 4999–5008.

[57] K. Zhang, Z. Zhao, X. Wang, Ni_2P/rGO as a highly efficient sulfur host toward enhancing the polysulfides redox for lithium-sulfur batteries, J. Alloys Compd. 906 (2022).

[58] W. Yao, W. Zheng, J. Xu, C. Tian, K. Han, W. Sun, S. Xiao, ZnS-SnS@NC heterostructure as robust lithiophilicity and sulfiphilicity mediator toward high-rate and long-life lithium–sulfur batteries, ACS Nano 15 (2021) 7114–7130.

[59] Y. Qiu, X.-J. Yin, M.-X. Wang, M. Li, X. Sun, B. Jiang, H. Zhou, D.-Y. Tang, Y. Zhang, L.-S. Fan, Constructed conductive $CoSe_2$ nanoarrays as efficient electrocatalyst for high-performance Li–S battery, Rare Metals 40 (2021) 3147–3155.

[60] H. Shao, W. Wang, H. Zhang, A. Wang, X. Chen, Y. Huang, Nano-TiO_2 decorated carbon coating on the separator to physically and chemically suppress the shuttle effect for lithium-sulfur battery, J. Power Sources 378 (2018) 537–545.

[61] X. Liang, A. Garsuch, L.F. Nazar, Sulfur cathodes based on conductive MXene nanosheets for high-performance lithium–sulfur batteries, Angew. Chem. 127 (2015) 3979–3983.

[62] S.B. Patil, H.J. Kim, H.-K. Lim, S.M. Oh, J. Kim, J. Shin, H. Kim, J.W. Choi, S.-J. Hwang, Exfoliated 2D Lepidocrocite titanium oxide Nanosheets for high sulfur content cathodes with highly stable Li–S battery performance, ACS Energy Lett. 3 (2018) 412–419.

[63] Y. Wang, Y. Xiong, Q. Huang, Z. Bi, Z. Zhang, Z. Guo, X. Wang, T. Mei, A bifunctional VS_2–Ti_3C_2 heterostructure electrocatalyst for boosting polysulfide redox in high performance lithium–sulfur batteries, J. Mater. Chem. A 10 (2022) 18866–18876.

[64] J. Shen, X. Xu, J. Liu, Z. Liu, F. Li, R. Hu, J. Liu, X. Hou, Y. Feng, Y. Yu, M. Zhu, Mechanistic Understanding of Metal Phosphide Host for Sulfur Cathode in High-Energy-Density Lithium–Sulfur Batteries, ACS Nano 13 (2019) 8986–8996.

[65] C. Yang, B. Zhang, J. Xiao, S. Jiao, H. Zhu, Effect of oxygen-substituted lattice carbon in Ti_3C_2 MXene as anchoring material for Li-S battery: DFT calculations and experiments, Appl. Surf. Sci. 677 (2024) 161007.

[66] Z. Ye, Y. Jiang, T. Yang, L. Li, F. Wu, R. Chen, Engineering catalytic CoSe–ZnSe heterojunctions anchored on graphene aerogels for bidirectional sulfur conversion reactions, Adv. Sci. 9 (2022) 2103456.

[67] X. Zuo, M. Zhen, D. Liu, H. Yu, X. Feng, W. Zhou, H. Wang, Y. Zhang, A multifunctional catalytic interlayer for propelling solid–solid conversion kinetics of Li_2S_2 to Li_2S in lithium–sulfur batteries, Adv. Funct. Mater. 33 (2023) 2214206.

[68] C. Barchasz, F. Molton, C. Duboc, J.-C. Leprêtre, S. Patoux, F. Alloin, Lithium/sulfur cell discharge mechanism: an original approach for intermediate species identification, Anal. Chem. 84 (2012) 3973–3980.

[69] Y.X. Yin, S. Xin, Y.G. Guo, L.J. Wan, Lithium–sulfur batteries: electrochemistry, materials, and prospects, Angew. Chem. Int. Ed. 52 (2013) 13186–13200.

[70] S.S. Zhang, Effect of discharge cutoff voltage on reversibility of lithium/sulfur batteries with $LiNO_3$-contained electrolyte, J. Electrochem. Soc. 159 (2012) A920.

[71] V.P. Nguyen, Y. Qureshi, H.C. Shim, J.M. Yuk, J.H. Kim, S.M. Lee, Intercalation-conversion hybrid cathode enabled by MXene-driven TiO_2/TiS_2 Heterostructure for high-energy-density Li–S battery, Small Struct. 5 (2024) 2400196.